Computers and Geosciences 124 (2019) 72–84

Contents lists available at ScienceDirect

Computers and Geosciences

journal homepage: www.elsevier.com/locate/cageo

Effective coal seam surface modeling with an improved anisotropy-based, multiscale interpolation method

Qingren Jia[a], Defu Che[a,b,*], Wenwen Li[c,1]

[a] College of Resources and Civil Engineering, Northeastern University, China
[b] Key Laboratory of Ministry of Education on Safe Mining of Deep Metal Mines, Northeastern University, China
[c] School of Geographical Sciences and Urban Planning, Arizona State University, USA

ARTICLE INFO

Keywords:
subsurface reconstruction
Coal seam modeling
Multiscale CSRBFs
Global anisotropy
Fault simulation

ABSTRACT

A reliable coal seam model is highly significant for mining design and resource assessment. However, due to the anisotropic nature of geological attributes, accurately modeling the surface using existing interpolation methods is difficult. Here, we propose a new method for coal seam surface modeling. First, we introduce a multiscale interpolation method using compactly supported radial basis functions (CSRBFs) and improve the modeling accuracy by anisotropy calculations using the raw mine data set. Then a fault modeling method is provided to simulate faults intersecting with coal seams. This method consists of three main parts: (1) anisotropy calculation to alleviate the effects of global anisotropy; (2) rapid coal seam surface modeling of large amounts of nonuniform data through an anisotropic multiscale CSRBF method and then visualization and organization of the surface into a triangulated irregular network (TIN); and (3) local reconstruction of the coal seam surface according to the faults. A prototype system was developed based on this method to build a coal seam model from the collected multisource coal seam data. A comparison with three existing interpolation methods shows that this method is feasible and time efficient and achieves higher accuracy than previous methods. We anticipate that the method can provide a reference for advances in digital and smart mines as well as 3D geological modeling.

1. Introduction

Coal seam surface modeling is required to fulfill the needs of coal boundary delimitation, natural resource evaluation, hazard assessment, and tunnel arrangement for coal mine planning (Caumon et al., 2009; Li et al., 2013). Studies regarding coal seam modeling cannot accurately reveal morphological surface variations of the coal seam throughout the mining process, which is insufficient to meet the increasing demand for a precise definition of subsurface conditions (Zhu et al., 2013). Multisource data from coal mine production activities, such as geological exploration, geological profiling, underground surveying and geological sketching, reveal coal seam surface variations in different areas and at different scales, and an effective surface modeling method is necessary to combine these different data (de Rienzo et al., 2008; Kaufmann and Martin, 2009; Lindsay et al., 2012; Bianchi Fasani et al., 2013). These findings suggest that nonuniform spatial data have become an important factor that affects the modeling results. A variety of interpolation methods have been applied to geological modeling to reconstruct surfaces from sampling points, such as discrete smooth interpolation (Caumon et al., 2009, 8; Collon et al., 2015), kriging (Hassen et al., 2016; Boisvert and Deutsch, 2011) and Bayesian geostatistical methods (Li et al., 2013).

Recently, implicit functions have been applied to this problem. These functions automatically extract the 3D surface from the scalar field in which the samples are distributed. In geological applications, the signed distance function (SDF) is widely used (Wilde and Deutsch, 2012). Many interpolation methods have been used to evaluate the SDF, including the kriging, inverse distance weight and radial basis function (RBF) interpolation methods. Among these methods, RBF is most commonly used in the geological modeling literature because of its simple mathematical form and high interpolation accuracy (Franke, 1982; Cowan et al., 2003; Hillier et al., 2014; Knight et al., 2007; Vollgger et al., 2015). However, when the number of points reaches thousands, computing the global RBF matrix will become very time consuming. The fast multipole method provided by Carr et al. (2001) and the local compact support RBF (CSRBF) method proposed by Turk

* Corresponding author. College of Resources and Civil Engineering, Northeastern University, Shenyang, 110819, China.
E-mail addresses: jqrneu@163.com (Q. Jia), chedefu@mail.neu.edu.cn (D. Che), wenwen@asu.edu (W. Li).

[1] Authorship Statement: Jia and Che initiated the idea, developed the methodology and conducted the experiments; Jia completed the first draft of the manuscript; Li provided input for revision and design of additional experiments; Li and Che reviewed and revised the manuscript.

https://doi.org/10.1016/j.cageo.2018.12.008
Received 8 November 2017; Received in revised form 18 December 2018; Accepted 20 December 2018
Available online 24 December 2018
0098-3004/

and O'Brien (2002) reduce the modeling time. Ohtake et al. (2003) further developed the CSRBF method using a multiscale method. A point set hierarchy is established based on an octree structure, and the CSRBFs are fit recursively. The multiscale CSRBFs can be solved quickly and used to reconstruct the 3D model from nonuniform data. Therefore, the multiscale CSRBFs have been applied to point cloud processing and many surface reconstruction studies.

The multiscale CSRBF method for a surface model is isotropic, which means that the geological attributes change at the same gradient in different directions of the 3D scalar field. However, the geographical attributes, which change based on many factors, will cause an anisotropic spatial field. The spatial interpolation method needs to consider the anisotropic characteristics of the geographical attributes to establish a model consistent with the process and spatial variation of the geographical attributes. Interpolations conditioned by anisotropy are advantageous when gradient data are sparsely and unevenly distributed, and such methods can enhance the structural geometry (Martin and Boisvert, 2017). Hillier et al. (2014) included a global anisotropy calculation using an anisotropic kernel in the interpolation process. However, this work is only capable of dealing with sparse data, and its computational efficiency is greatly challenged when the data size to be interpolated increases.

In this paper, we propose an anisotropic multiscale CSRBF method for coal seam surfaces modeling and reconstruction the coal seam surface model from multisource data. A fault modeling method on the coal seam surface is also given. This method takes advantages of both the time efficiency and scalability of the multiscale CSRBF method (i.e., Ohtake et al., 2003) and the ability to handle spatially uneven data distributions of the anisotropy-based approach (i.e., Hillier et al., 2014). The results prove that our method can improve both the modeling accuracy and computational efficiency based on experimental data collected in the Qianjiaying coal mine located in Tangshan, China. Finally, the coal seams and faults in the Qianjiaying coal mine are modeled and visualized.

2. Geological context and data sources

The Qianjiaying coal mine is located approximately 15 km southeast of Tangshan, China and has an area of 88 square kilometers. There are 8 coal layers (5, 6 1/2, 7, 8, 9, 11, 12-1 and 12-2) available in the field. The structure of the coal mine is mainly composed of folds supplemented by faults (Fig. 1).

2.1. Regional geological and geophysical survey data

There are 259 exploration boreholes and 26 main faults in this area, of which 6 faults are located in the throw range of 50–30 m, 7 faults are in the range of 30–10 m, and the others are below 10 m. In this paper, the 10th mining region of 7 coal seams is selected as the study area (3.5 km × 2.7 km), including 26 boreholes and 43 faults (Fig. 2, throw of fault > 1.0 m).

2.2. Local observations obtained in the mining process

We collected coal seam location data from the excavation stage and mining stage, including underground survey data, downhole drilling data and geological sketch data. Survey points (985) and underground boreholes (57) were collected in the study area, and 1410 sketch points are from the 2074E mining area, and they are all shown in Fig. 2. For data confidentiality, all coordinates are offset by the location of the vertical shaft in the Qianjiaying coal mine.

3. Methodology

3.1. Method overview

The overall workflow is illustrated in Fig. 3 and consists of four main steps. The major coal seam surface modeling steps are described as follows.

1. Data collection and preprocessing. Discrete points are extracted from multisource data. Then, the normal vectors of the points are obtained using the Point Cloud Library (PCL) (Rusu and Cousins, 2011).
2. Global anisotropy calculation. The orientation matrix is constructed from normal vectors found within defined neighborhoods, and two main directions for the coal seam in the scalar field are given. The RBFs will no longer be radial through global anisotropic transformations, and the global anisotropy can be incorporated with the interpolations.
3. Coal seam surface modeling. The multiscale CSRBF method is applied to the points and their normal vectors. A coarse-to-fine point set hierarchy is established, and the CSRBFs of each point set are calculated gradually. Global anisotropy is added to the implicit method to eliminate anisotropic effects by matrix transformation and to obtain better results. A visualization of the implicit surface is performed by Blumenthal's polygonizer (Bloomenthal, 1988; Narayan et al., 2015), and the final surface is transformed into TIN for visual display.
4. Fault simulation in a coal seam model. The centerline of the fault on the TIN is calculated from the collected fault data. The influence domain of the single fault is calculated, and then the coal seam is separated within this domain to complete the fault construction by local triangulation.

3.2. Multiscale CSRBF method

Given a set of N points $\rho = \{\boldsymbol{p}_i\}$ scattered along a surface, the RBF fits a function to a scalar field $F(\boldsymbol{x})$ that is sampled at ρ (Fasshauer and Gregory, 2007). $F(\boldsymbol{x})$ is defined by a monotonic volumetric function $f(\boldsymbol{x}) = f$, and its zero level-set $f = 0$ interpolates ρ. The scalar field is separated into two parts by the implicit surface $f(\boldsymbol{x}) = 0$: $f(\boldsymbol{x}) > 0$ and $f(\boldsymbol{x}) < 0$. Then, the CSRBF expression is defined as follows:

$$f(\boldsymbol{x}) = \sum_{\boldsymbol{p}_i \in \rho} \Psi(\boldsymbol{x}) = \sum_{\boldsymbol{p}_i \in \rho} [g_i(\boldsymbol{x}) + \lambda_i]\phi_\sigma(\|\boldsymbol{x} - \boldsymbol{p}_i\|), \tag{1}$$

where $\phi_\sigma(r) = \phi(r/\sigma)$ is a compact support RBF, σ is the support size, $g_i(\boldsymbol{x})$ is defined at each point p_i, its zero level-set $g_i(\boldsymbol{x}) = 0$ approximates the shape of ρ in a small vicinity of $\boldsymbol{p}_i$ by a quadric

$$w = h(u, v) = Au^2 + 2Bvu + Cv^2,$$

where A, B, and C are determined by a minimization of the least squares

$$\sum_{(u_j, v_j, w_j) = \boldsymbol{p}_j \in \rho} \phi_\sigma(\|\boldsymbol{p}_j - \boldsymbol{p}_i\|)(w_j - h(u_j, v_j))^2 \rightarrow min.$$

Then, we obtain the following:

$$g_i(\boldsymbol{x}) = w - h(u, v).$$

The coefficient λ_i is determined from the interpolation conditions:

$$\sum_{\boldsymbol{p}_i \in \rho} \lambda_i \phi_{ij} = -\sum_{\boldsymbol{p}_i \in \rho} g_i(\boldsymbol{p}_j)\phi_{ij},\ \phi_{ij} = \phi_\sigma(\|\boldsymbol{p}_j - \boldsymbol{p}_i\|).$$

An octree-based spatial index to hierarchically partition and organize the point sets is built to increase the computational efficiency of the RBFs (see an illustration in Fig. 4). The process starts with a single region surrounding all given points (the root node) and then recursively sub divides the region into its 8 octree regions (the internal nodes). The recursion ends when the number of sampling points in the node is not

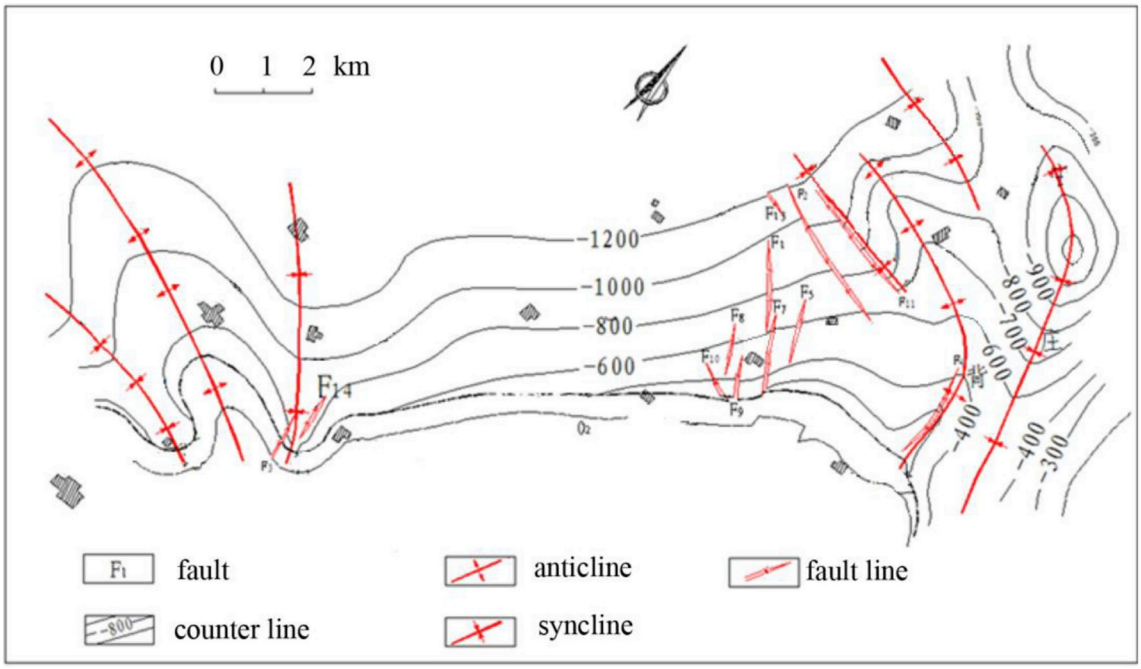

Fig. 1. Geological structure map of Qianjiaying coal mine (2-column).

more than eight (leaf nodes). Thus, points with different densities are included in different levels to construct hierarchical point sets, and the support radius σ can be obtained from the size of a region, i.e., the node of one level in the octree, which will positively affect the result of the CSRBF interpolation.

After the construction of the octree, the centroid parameters for each node, including the position and normal vector, are then calculated, and the hierarchical point set $\{\rho^1, \rho^2, ..., \rho^M = \rho\}$ is constructed based on the levels of the octree.

Then, the interpolation model is constructed in a coarse-to-fine manner. An initial value of function is set as follows:

$$f^0(\boldsymbol{x}) = -1,$$

Then, the set of interpolating functions are recursively defined as follows:

$$f^k(\boldsymbol{x}) = f^{k-1}(\boldsymbol{x}) + o^k(\boldsymbol{x}),\ k = 1,2,\ ...,\mathrm{M},$$

where $f^k(\boldsymbol{x}) = 0$ interpolates ρ^k, and $o^k(\boldsymbol{x})$ has the same form as Eq. (1).

3.3. Integrating global anisotropy into the multiscale CSRBF method to handle spatially anisotropic distributed mining data

To construct an anisotropic interpolation model, the anisotropy in the scalar field must be estimated, which means that the main orientations of the attribute changes must be identified, and then the interpolator is spatially transformed. Such information is recorded in the transformation matrix used in the interpolation method, such as Ordinary Kriging (OK). The acquisition of such information often requires a manual review and identification process by geologists. Hence, it cannot be performed using an automatic manner method, such as OK.

To overcome this limitation, we further integrate the vector defining the structural anisotropy (Hillier et al., 2014) for an automatic global anisotropy calculation. Mathematically, it can be derived from an Eigen analysis of the orientation matrix,

$$\begin{bmatrix} \sum_j^k n_{jx}^2 & \sum_j^k n_{jx}n_{jy} & \sum_j^k n_{jx}n_{jz} \\ \sum_j^k n_{jy}n_{jx} & \sum_j^k n_{jy}^2 & \sum_j^k n_{jy}n_{jz} \\ \sum_j^k n_{jz}n_{jx} & \sum_j^k n_{jz}n_{jy} & \sum_j^k n_{jz}^2 \end{bmatrix}, \tag{2}$$

which is formed by the k normal vectors $\boldsymbol{n}_j$ found in the defined neighborhood. The Eigen analysis yields the eigenvalues, $E1$, $E2$ and $E3$,

$E1 < E2 < E3$,

and the matrix of eigenvector

$$V = \begin{bmatrix} v_{1x} & v_{2x} & v_{3x} \\ v_{1y} & v_{2y} & v_{3y} \\ v_{1z} & v_{2z} & v_{3z} \end{bmatrix},$$

where $\boldsymbol{v}_1$, $\boldsymbol{v}_2$, and $\boldsymbol{v}_3$ are associated with the obtained eigenvalues $E1$, $E2$ and $E3$, respectively.

These eigenvectors locally define the main directions of anisotropy. Here, we calculate the anisotropy to achieve a higher accuracy in reconstructing the coal seam surface.

When performing a CSRBF interpolation for data at each hierarchical level of the spatially organized octree, Wendland's compactly supported RBF with a C2-continuous function in a 3D scalar field is used (H. Wendland, 1995):

$$\phi(r) = (1-r)_+^4(4r+1).$$

Global anisotropy can be included in the interpolation using the translation invariant basis function of the form $(\boldsymbol{x}, \boldsymbol{x}') = \varphi(\boldsymbol{x} - \boldsymbol{x}')$, which means that the RBFs are not radial anymore. This new basis function can be constructed by a global orientation matrix (Eq. (2)) containing all planar orientation data, and an anisotropic distance can be calculated:

$$r = \sqrt{\frac{(x-x')_{trans}^2 + (y-y')_{trans}^2 + (z-z')_{trans}^2}{\sigma^2}}, \tag{3}$$

where

$$\begin{bmatrix} (x-x')_{trans} \\ (y-y')_{trans} \\ (z-z')_{trans} \end{bmatrix} = VSV^T \begin{bmatrix} (x-x') \\ (y-y') \\ (z-z') \end{bmatrix} \tag{4}$$

The scaling matrix S is defined as follows:

$$S = \begin{bmatrix} 1 & 0 & 0 \\ 0 & \sqrt{E2/E1} & 0 \\ 0 & 0 & \sqrt{E3/E1} \end{bmatrix}$$

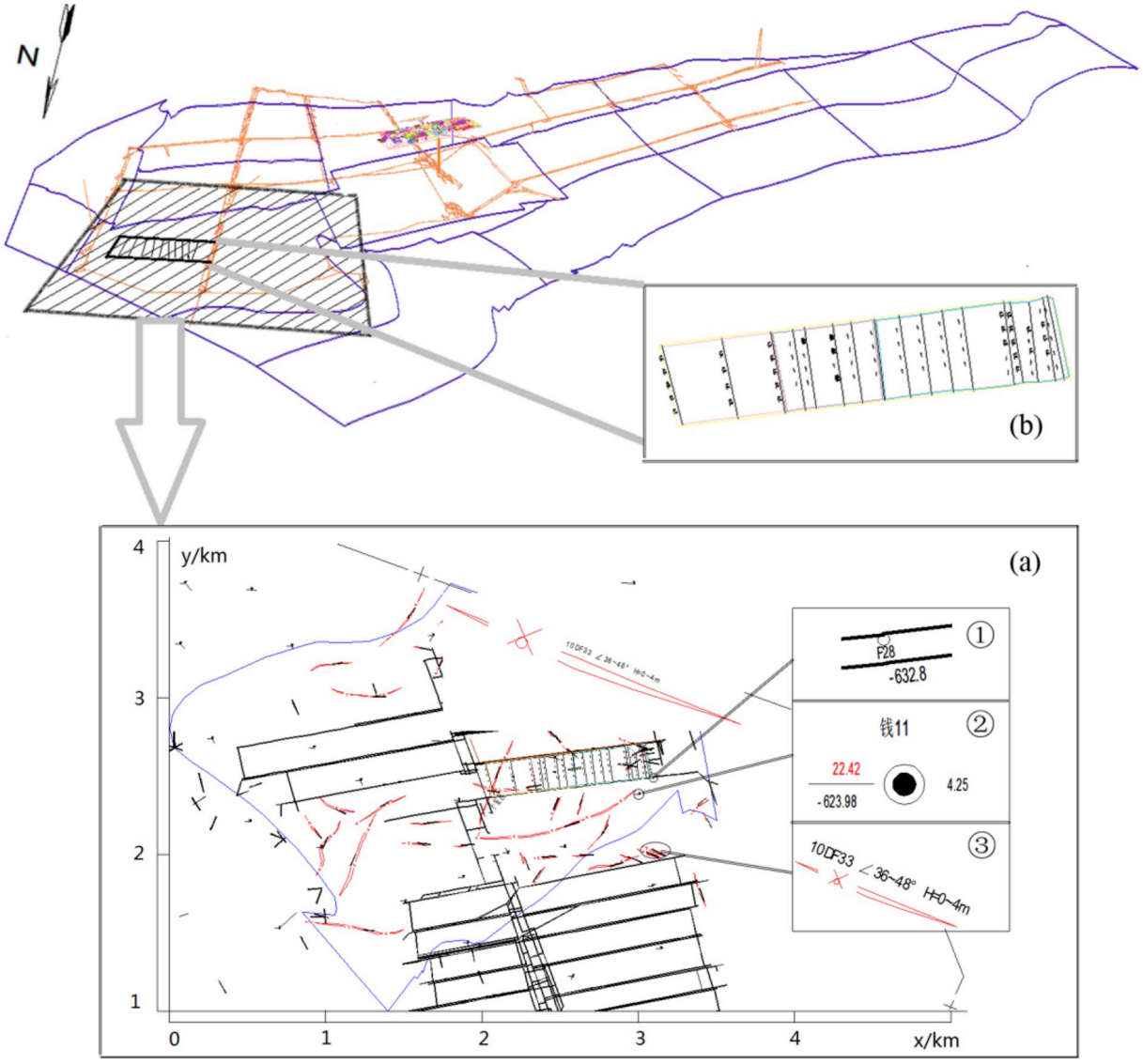

Fig. 2. Overview of test area illustrating (a) multisource data, including ①underground surveying data, ②drill data, ③fault data, and (b) geological sketch line data in 2074E mining area. (2-column).

Anisotropy is the property of scalars that are directionally dependent in a scalar field, and it is opposite of isotropy. Here, the scalars refer to the coordinates of sampling points. Therefore, the global anisotropy matrix is not performed on normal vectors.

3.4. Fault simulation

Faults result from the destruction of the original structure by geological processes and are one of the most important geologic structures for coal seam modeling (Guo et al, 2016). Therefore, it is necessary to simulate faults and reconstruct the coal seam surface model in the fault domain.

The continuous triangle generated by the Delaunay criterion can express complex surfaces accurately, offering the best surface simulation. Therefore, we can transfer the triangles from the visualization of the implicit function onto the TIN structure and then propose a TIN-based fault modeling method. The original fault data are from drills or geological sketches and include tendency, inclination, and throw.

3.4.1. Fault centerline on a coal surface

A fault centerline is derived from an observation point set $\{O_i\,(x_i, y_i, z_i),\ i = 1, \ldots, n\}$ of fault f, and the point set is extended to obtain starting point O_0 and ending point O_{n-1}. For each point, we have dip direction α, dip angle β, throw parameter h and a three-dimensional coordinate. To obtain $O_{n+1}\,(x_{n+1}, y_{n+1}, z_{n+1})$, we have $O_n\,(x_n, y_n, z_n)$ and

$$\begin{bmatrix} x_{n+1} \\ z_{n+1} \end{bmatrix} = \begin{bmatrix} x_n \\ z_n \end{bmatrix} - \begin{bmatrix} 0 \\ h \end{bmatrix} + L \begin{bmatrix} \cos(\alpha + \pi/2) \\ 0 \end{bmatrix} \begin{matrix} y_{n+1} \\ \end{matrix} = \begin{matrix} y_n \\ \end{matrix} - \begin{matrix} 0 \\ \end{matrix} + L \begin{matrix} \sin(\alpha + \pi/2) \\ \end{matrix},$$

where $L = ch$ and c = 1.5 is a linear profile (Cowie and Shipton, 1998) of f that extends O_n to O_{n+1} (Fig. 5b).

Then, all points are projected to TIN to get an ordered points array $O = \{O'_i\,(x'_i, y'_i, z'_i),\ i = 0, \ldots, n + 1\}$ of fault centerline. The ray-triangle intersection algorithm (Moller and Trumbore, 2005) is implemented to get O (Fig. 6).

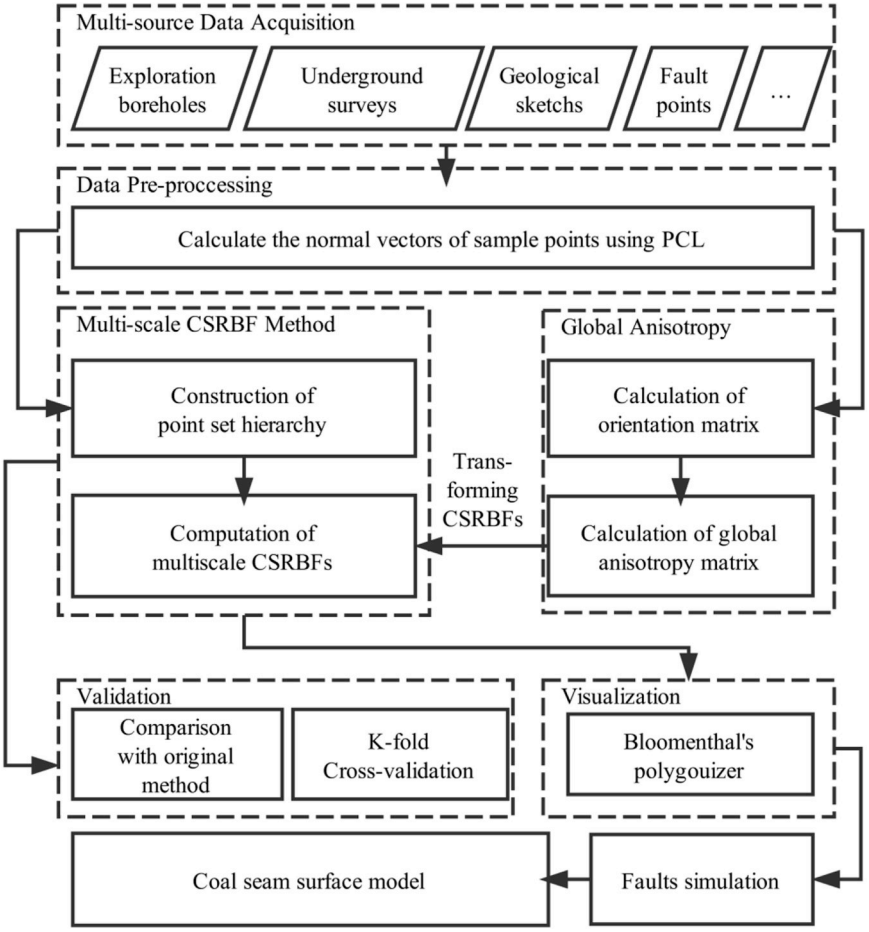

Fig. 3. Workflow of anisotropic multiscale CSRBF method for coal seam surface modeling (2-column).

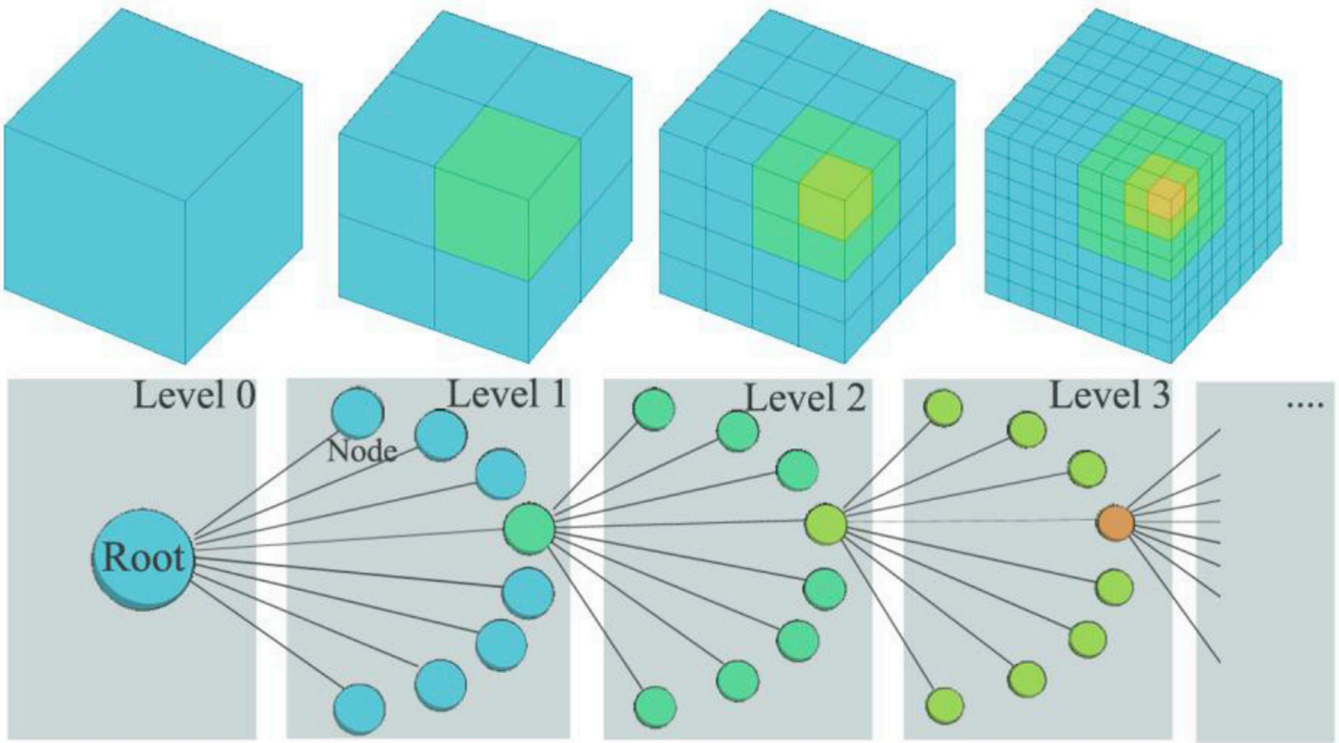

Fig. 4. Spatial partitioning based on octree: each node will be divided into eight equal-sized child nodes in next partition (2-column).

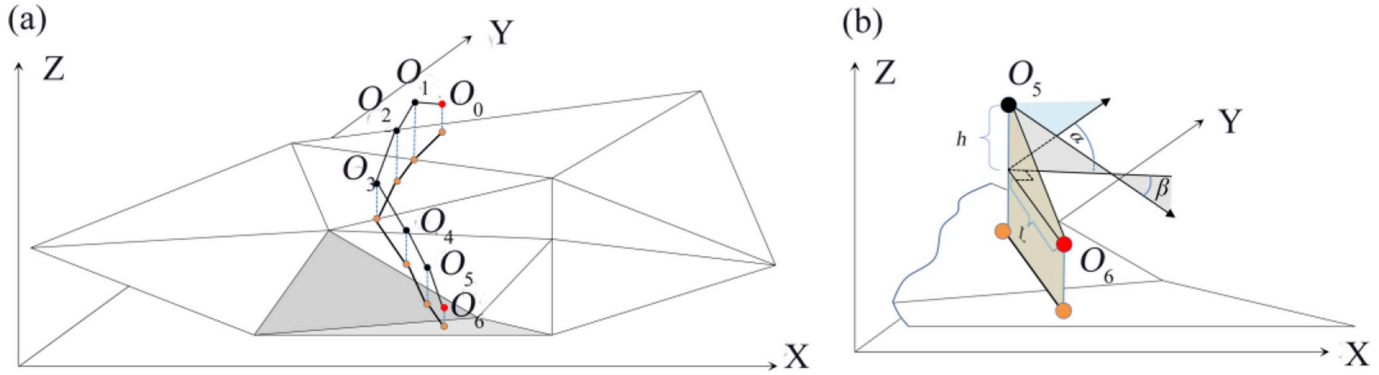

Fig. 5. Calculation of fault ending position through observations, (a) position of fault observations and TIN, and (b) calculated coordinates of fault ending position (red) from observation point (black) (2-column). (For interpretation of the references to colour in this figure legend, the reader is referred to the Web version of this article.)

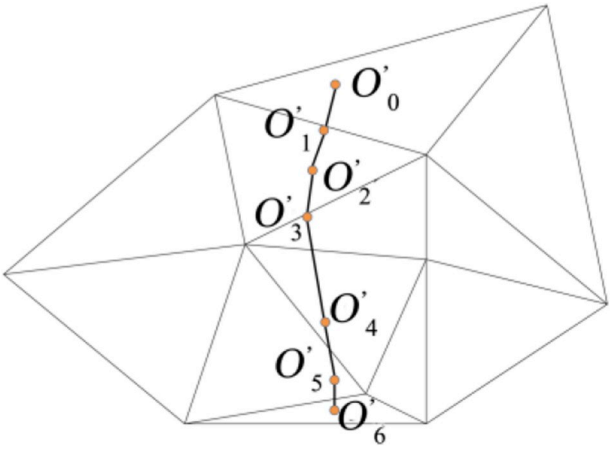

Fig. 6. Fault centerline on TIN (1-column).

3.4.2. Local fault triangulation

The intersection line between a fault and coal seam, which is referred to as the interline, is typically defined by two parts: the up-interline, which is the fault that intersects the hanging wall, and the down-interline, which is the fault that intersects the footwall.

After confirming the displacement range of the fault by the fault centerline, the local triangular mesh around the centerline is reconstructed. As illustrated in Fig. 7a, p_0 is the pinch-out point of fault f located in a triangle contained by p_1, p_2, p_3. The triangle is reconstructed into three new triangles in Fig. 7b. Then, the triangles in the fault displacement range are removed, and the up and down boundaries are identified (Fig. 7c).

A local fault triangulation algorithm is proposed and executed next. The reconstruction algorithm is similar to that produced by Tsai by inserting a constraint segment into a Delaunay triangulation network (Tsai, 1993), and it can be applied to concave polygons. For the normal fault, reconstruction is executed in the region surrounded by the up-boundary and up-interline and similarly for the down-boundary and down-interline (Fig. 8a). In contrast, for the reverse fault, the reconstruction is executed in the area surrounded by the up-boundary and down-interline and the down-boundary and up-interline (Fig. 8b). The pseudo code is listed in Appendix A.

The function “LOPswapping” in line 42 is a locally optimal diagonal function for a convex quadrilateral consisting of two adjacent triangles (Lawson, 1977), and “Intersect” is a function to judge whether the line segments intersect. A detailed code is not given here.

4. Results from a case study: coal seam surface modeling in the Qianjiaying coal mine

We developed a prototype system based on our modeling method. Three-dimensional coal seam models were created based on real regional geological data in this system. The testing area contained 2478

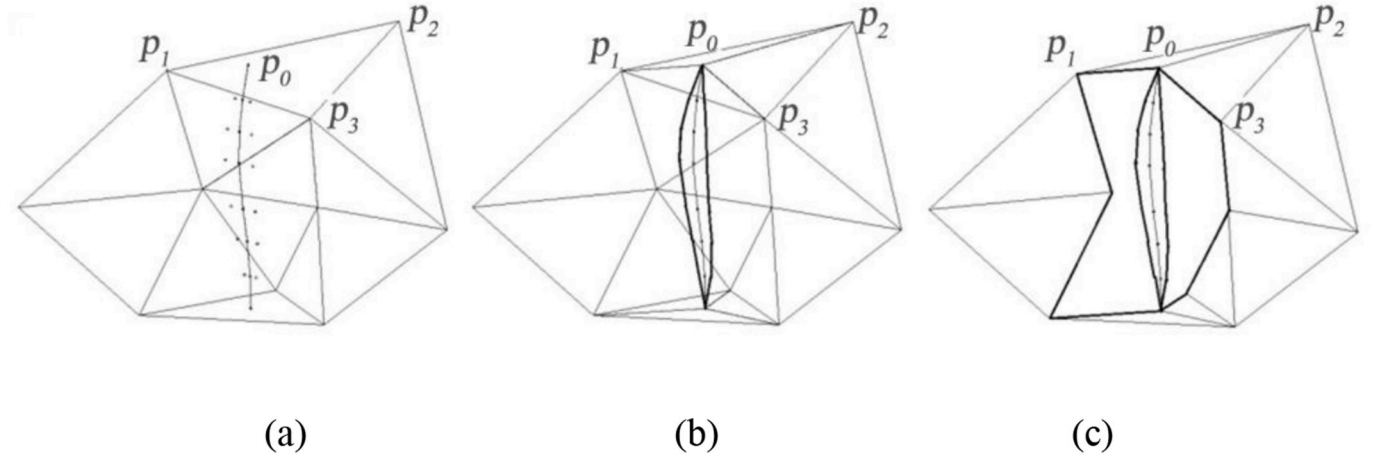

Fig. 7. Local fault triangulation, (a) fault centerline on calculated coal fault, (b) fault displacement range calculation, and (c) removing triangles that intersected with displacement boundaries (2-column).

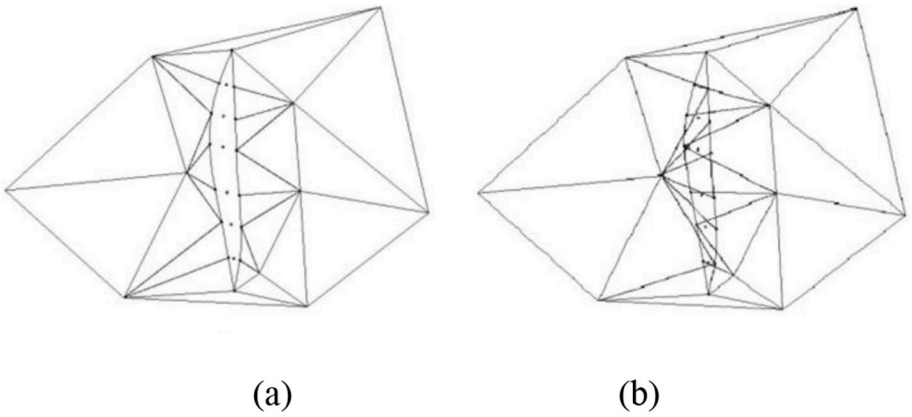

Fig. 8. Simulation results of faults: (a) normal fault and (b) reverse fault (2-column).

observations from multisource and multiscale data, and the basic modeling elements in the system were created, including coal surfaces and attitudes. Additionally, typical geological structures, such as faults, were also simulated on the surface models. Our experiments were performed on a ThinkPad laptop (2.5-GHz Intel(R) core (TM) i5-4200M, 4 GB of RAM memory, and an Intel HD graphics card).

4.1. Implicit surface modeling

A total of 2478 observation points and 43 faults were involved in our calculations, and the coal surface model was reconstructed based on these points.

4.1.1. Normal vectors and anisotropy computations

According to section 3.3, to include global anisotropy, we first need to obtain the normal vector of each point. The Point Cloud Library (PCL) was used to calculate the normal vectors of the sample points, and each normal vector was computed from 20 neighborhoods searched by the function *nearestKSearch()* (Hsieh and Cheng-Tiao, 2012). The results are illustrated in Fig. 9 using black lines.

Using these normal vectors, the global anisotropy translation matrix was calculated in *XY* space, and the CSRBFs were calculated with the translation matrix to reduce the impact of anisotropy. Thus, the coordinates of sample points were transformed as shown in Eq. (4), where

$$VSV^T = \begin{bmatrix} 1.039 & -0.228 \\ -0.228 & 2.350 \end{bmatrix},$$

The supporting size of the CSRBFs in the first layer was calculated by $\sigma = cL$, where L is the length of a diagonal of the bounding parallelogram. In addition, parameter c is 0.75 (Ohtake et al., 2003) and σ is 6571.837 m in the first layer and $\sigma/2^{k-1}$ in layer k.

The spatial variability in the elevation distribution of the sample points was analyzed through the GeoR library, and variograms were obtained in four directions (0, 45, 90 and 135°) as shown in Fig. 10. Fig. 10a shows that the elevation distributions showed significant anisotropy in 4 directions. For comparison, Fig. 10b shows the experimental variance functions of the data after global anisotropic transformation in the 4 directions, and the results show that anisotropy is alleviated.

Additionally, Fig. 11 illustrates the differences between the multiscale CSRBF method and the improved anisotropy-based version when a new position P was interpolated using this point set and the coordinates of the points centered with P were transformed using the transformation matrix VSVT, which means that the points selected to interpolate the CSRBFs were more evenly distributed, which led to a better interpolation result than the multiscale CSRBF method.

4.1.2. Calculation of multiscale CSRBFs

All sample points are divided into 7 hierarchical data sets based on the octree. Fig. 12 shows all 7 multiscale point sets. The last point set

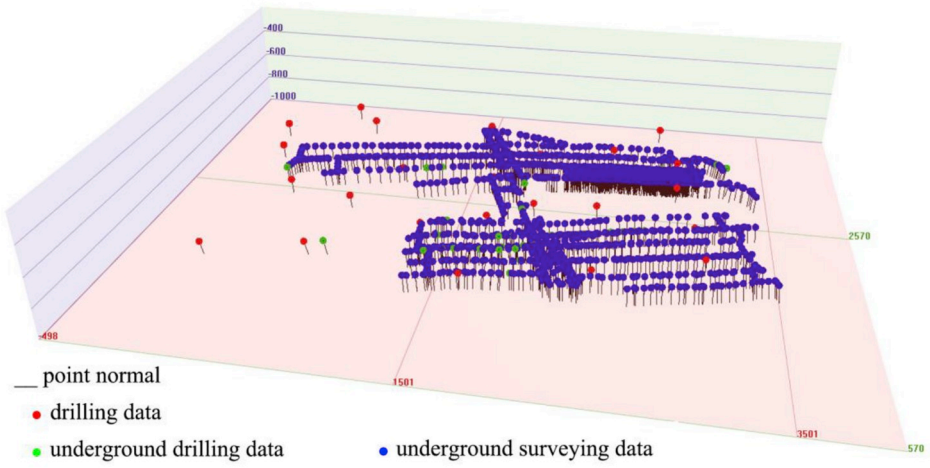

Fig. 9. Plot of sample points and normal vectors. Red dots show drilling locations, green dots show downhole drilling locations; blue dots indicate underground survey or geologic sketch locations; and black line segments identify normal vectors at each location (2-column). (For interpretation of the references to colour in this figure legend, the reader is referred to the Web version of this article.)

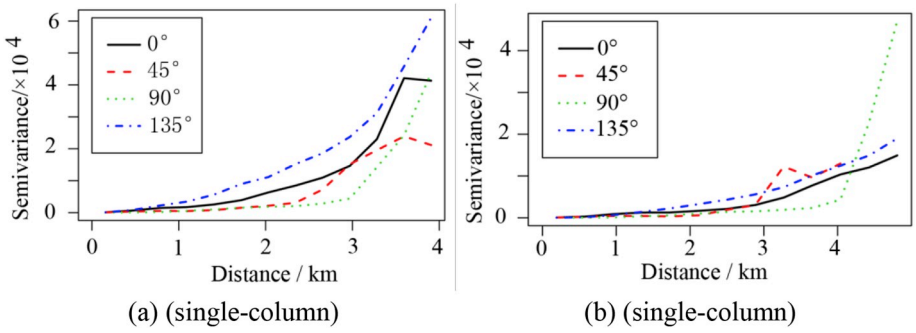

Fig. 10. Experimental variance functions in 4 directions: (a) based on original data and (b) based on data after location transformation.

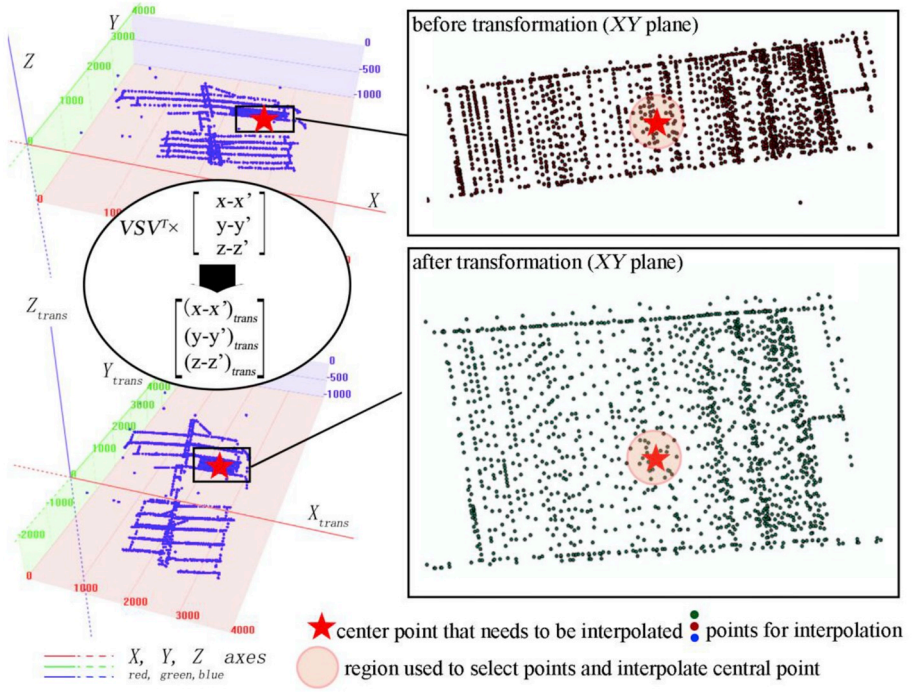

Fig. 11. Point distribution before and after anisotropy transformation (2-column).

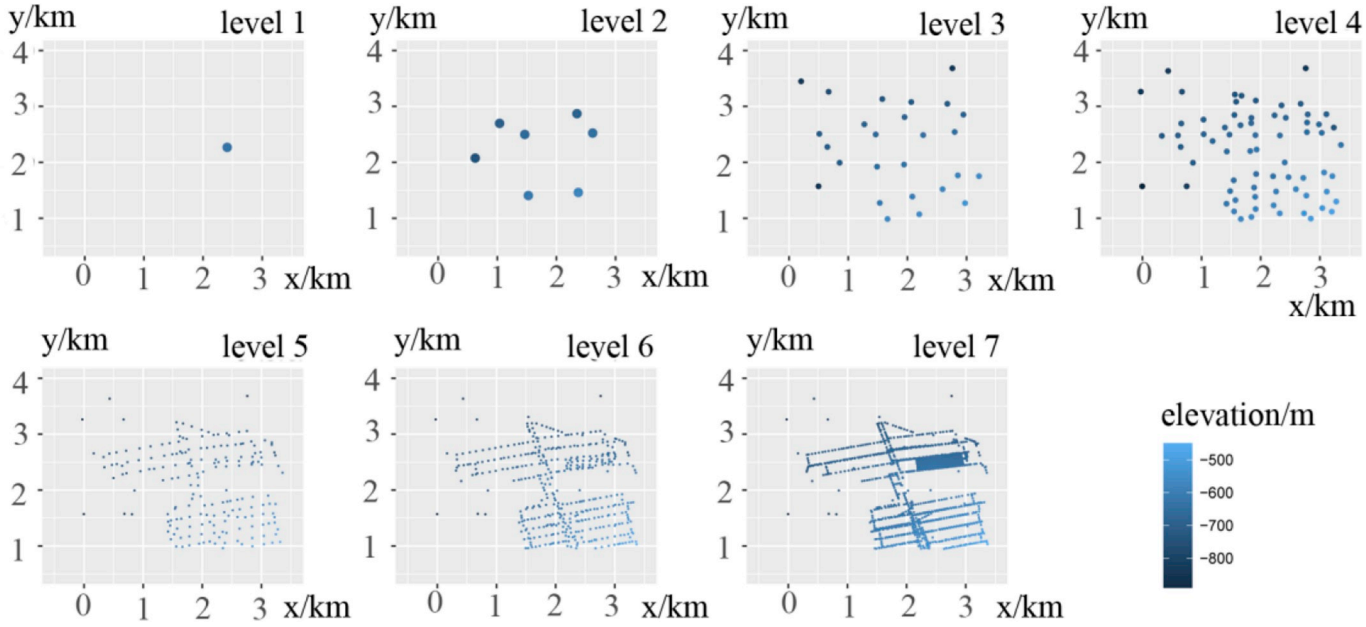

Fig. 12. Plots of 7 hierarchical levels of point sets (2-column).

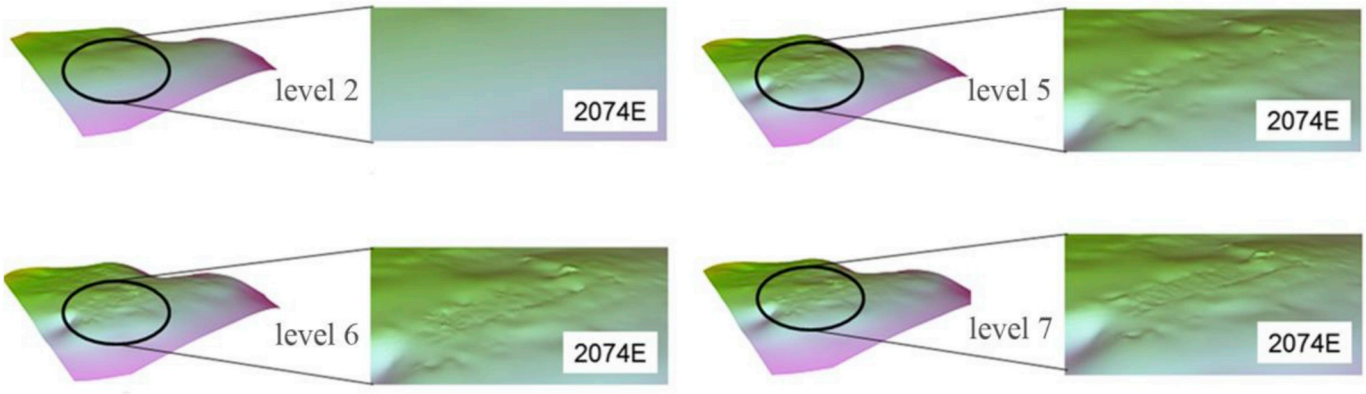

Fig. 13. Visualization of 2nd, 5th, 6th, and 7th levels of data sets (2-column).

includes all the point data used to calculate the CSRBF and confirm the final implicit function. The regional coal seam surface was then created based on our proposed multiscale CSRBF method with anisotropy.

4.1.3. Visualization of implicit surfaces

The implicit function was visualized for different point sets in Fig. 13. The global view of the visualized study area is illustrated on the left (a, c, e, and g), and the local area (2074E mining area) is on the right and enlarged to show more details (b, d, f, and h). By contrast, we can conclude that as the data set changes from the regional scale to the local scale and as the local density of sample data gradually increases, more details are modeled and illustrated.

4.2. Simulation of faults

The visualized coal seam surface is reorganized to be a TIN surface, where the faults are simulated locally. Fig. 14 shows the results of two reverse faults (F11 and F17) that are modeled based on section 3.4. From the 2D contours in Fig. 14a, the coal seam is locally reconstructed by the two faults. Fig. 14b and c show the effect of the fault simulation: coal seam TIN surface is separated by two faults.

Finally, the coal seam surfaces and faults in the Qianjiaying coal mine were simulated based on the proposed method (Fig. 15).

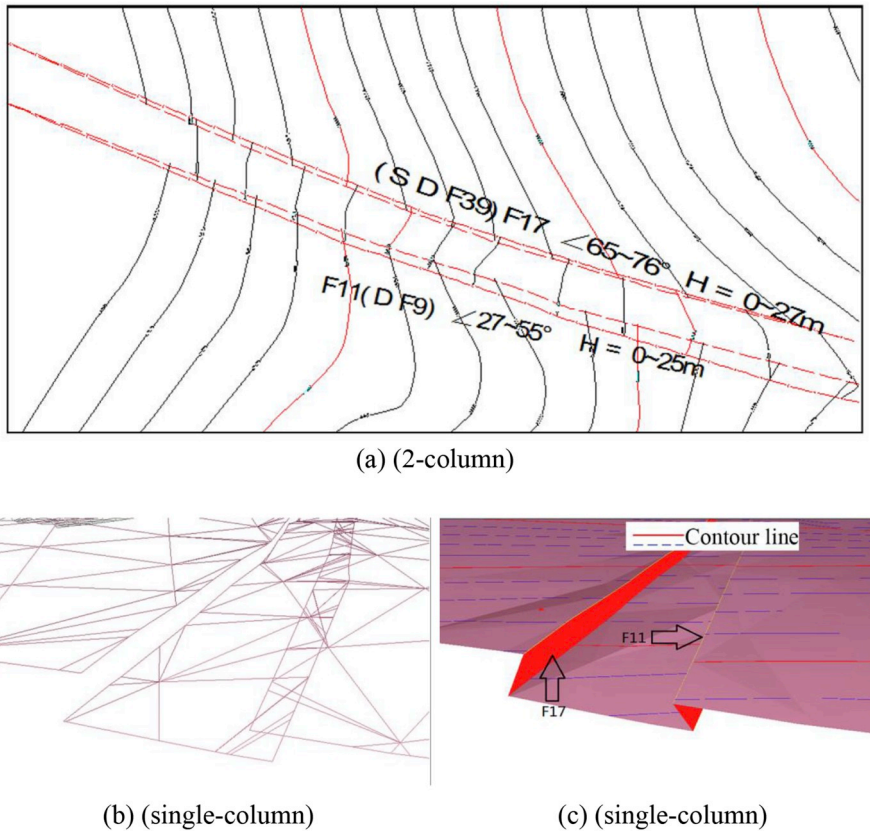

Fig. 14. Simulations of two reverse faults (a) in a 2D view with contours, (b) in a 3D frame view, and (c) in a 3D surface view.

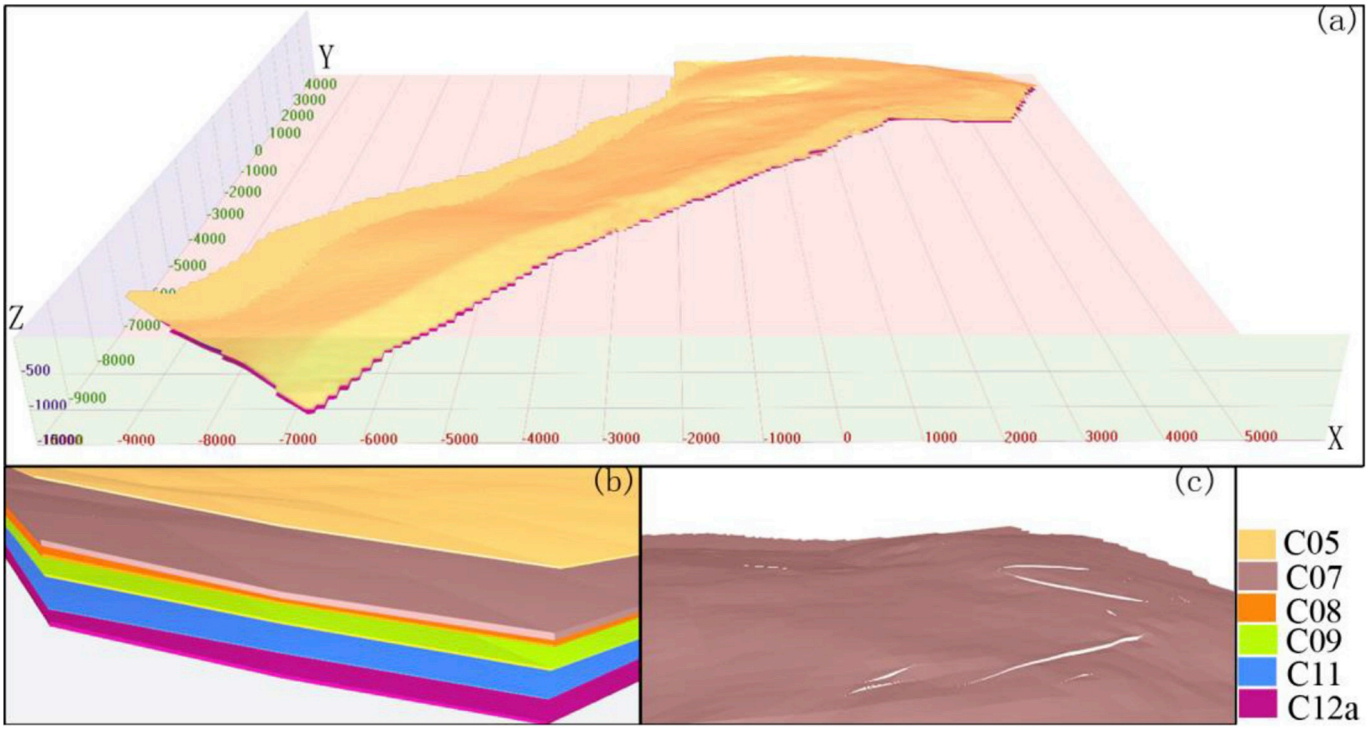

Fig. 15. Construction of coal surfaces and faults: (a) coal seam surface models Qianjiaying coal mine, (b) detail of models, and (c) C07 coal seam surface model with discontinuous topology caused by faults (2-column).

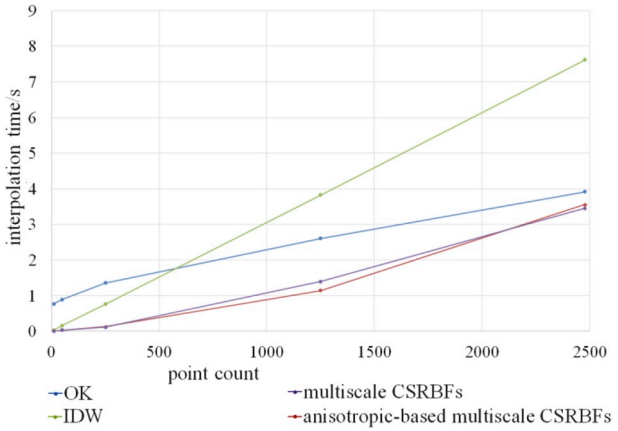

Fig. 16. Comparison of time efficiency as the number of sample points increases (2-column).

4.3. Comparison with other interpolation methods

Two experiments were used to verify the advantages of computational efficiency and interpolation accuracy. The inverse distance weighting (IDW) method and the Ordinary Kriging (OK) method were implemented, and the results were compared with those of the multiscale CSRBF method and our anisotropy-based multiscale CSRBF method.

In experiment 1, point sets containing different numbers of sampling points (10, 50, 250, 1250, 2478 points in each set) are used for interpolation. The variogram function fitted with the OK method is the Gaussian model, and the number of points in each interpolation is limited to 8 or less. The results show the two multiscale CSRBF methods used less time and presented a gradual increase of interpolation time as the number of sample points increased, whereas the interpolation time increased more rapidly with the IDW and OK methods. The interpolation time between the multiscale CSRBF method and our anisotropy-based multiscale CSRBF method are nearly equivalent (Fig. 16).

Table 1
Error statistics result from four interpolating methods based on a cross-validation.

	Error/m	Standard deviation/m
Method A	18.390	25.043
Method B	1.012	3.841
Method C	0.943	1.923
Method D	0.904	1.852

Note: method A: IDW, B: OK, C: multiscale CSRBF, and D: anisotropic-based multiscale CSRBF.

In experiment 2, a K–fold cross-validation (K = 10) is subsequently implemented for all four methods. The sampling points are divided into 10 subsets, of which 9 are used as modeling data and the other set is used as test data. The error in the absolute value of elevation between the interpolated attribute and the original position of sampling point is defined to represent the accuracy of the interpolations, and the standard deviation of the error indicates the stability of the interpolations.

The data set involved in the experiment contains 2478 points and their unit normal vectors, and the results (Table 1) indicate that our improved anisotropic multiscale CSRBF method achieves higher accuracy than the other methods. The IDW and OK methods present larger errors when the data are sparse, and the anisotropy method achieves the highest accuracy with a maximum of 22.015 m (the multiscale CSRBF, OK and IDW methods achieve values of 81.907 m, 209.595 m and 262.662 m, respectively, Fig. 17). In contrast with IDW and OK methods, both two CSRBF methods use the normal vector as a constraint in addition to the point coordinates, which leads to an improvement in the modeling and representation of geologic surfaces. Moreover, the improved anisotropy-based multiscale CSRBF method

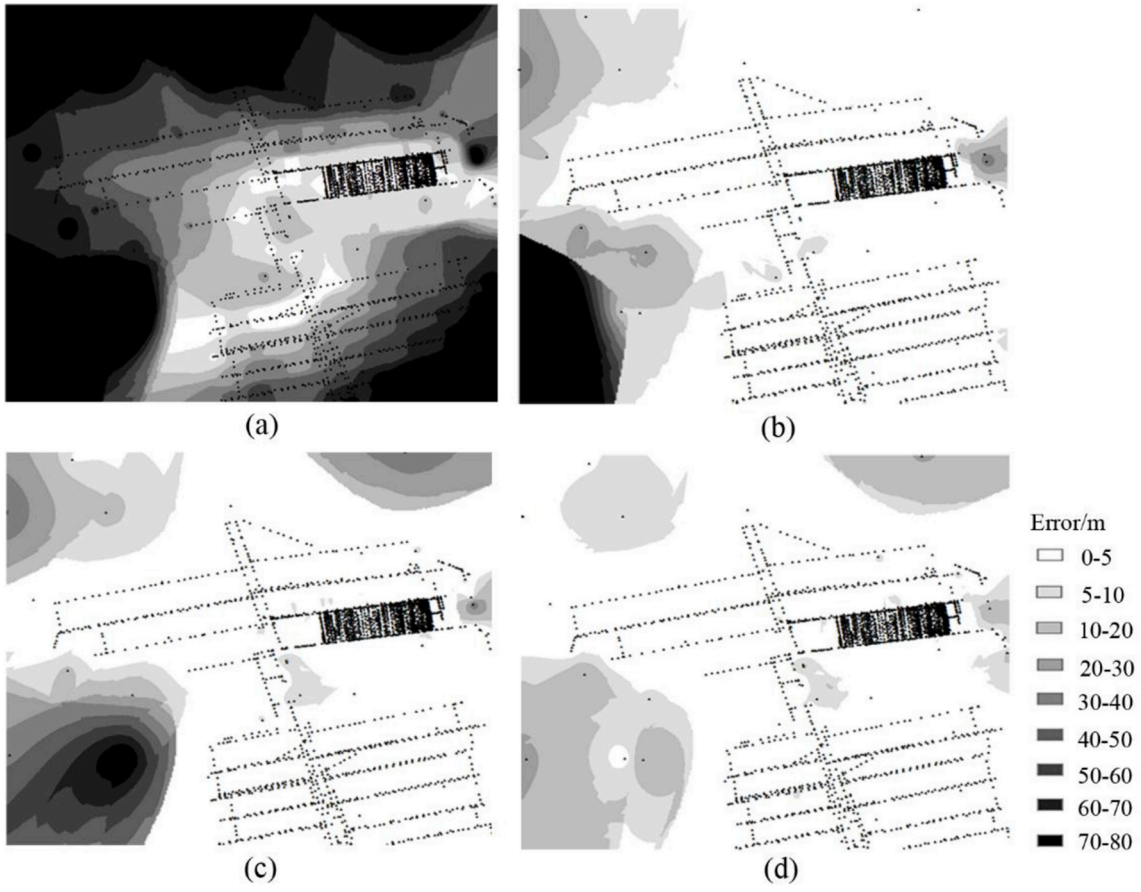

Fig. 17. Error distribution of cross-validation corresponding to (a) IDW method, (b) OK method, (c) multiscale CSRBF method and (d) improved anisotropic-based multiscale CSRBF method from left to right, top to bottom. (2-column).

represents an advancement because it considers the anisotropy of the coal seam spatial distribution compared with the original multiscale CSRBF method.

5. Conclusion and discussion

The multiscale CSRBF method performs well during rapid surface reconstructions with nonuniform data and coarse-to-fine computations. In this paper, we applied this method to coal seam surface modeling and updated the original multiscale CSRBF modeling process by considering anisotropy. The interpolation results of the Qianjiaying coal mine showed that our approach can provide more accurate interpolation surfaces. Additionally, we presented a practical fault modeling method for coal seam surfaces.

Compared to previous studies, the unique contributions of this research are as follows.

1. An improved anisotropic multiscale CSRBF method is applied to interpolate coal seam surface models automatically by constructing hierarchical point sets from discrete points. Manual interventions are not needed in the interpolation process. Therefore, this method advances the automatic modeling of coal seams from multisource geometric data distributions.
2. The comparison and cross-validation results show that our improved anisotropic-based multiscale CSRBF method has better accuracy than the multiscale CSRBF, IDW and OK methods and is more time efficient than the IDW and OK methods. These findings demonstrate the superior performance of the approach.
3. An improved fault 3D modeling method based on local TIN reconstruction is implemented to model topology discontinuities on the coal seam.

This method interpolates coal seams with location and normal data related to data points, and it does not involve other constraints, such as boundaries and off-contact constraints of the geological interface. For the current data set with thousands of points, interpolation can be executed quickly, whereas for large data sets with millions or even larger amounts of points, the construction and calculation of a RBF coefficient matrix will be very time consuming.

Acknowledgements

This work was conducted with support from the National Natural Science Foundation of China (Grant Nos. 41871310) and the Fundamental Research Funds for the Central Universities (Grant No. N160106002, N17241004). The authors are also grateful to the Qianjiaying Coal Mine for funding this research.

Appendix A

```
// input: lineA ~ one line in the fault
//        boundLinePointArray ~ points on the boundary line
// output: a Boolean value indicating whether the line intersects the boundary
Function Intersects(lineA, boundLinePointArray)
  for i in 0: boundLinePointArray.size
  lineB <- line(boundLinePointArray[i], boundLinePointArray[i + 1])
  if Intersect(lineA, lineB)
    return TRUE
  return FALSE

// input: boundLinePointArray ~ points on the boundary line
//          iBegin ~ start position on boundLinePointArray
//          pointA, pointB ~ two fault points
// output: pointA, BoundLinePointArray[iIndex],pointB: index of max angle with points
Function FindMaxAngle(boundLinePointArray, iBegin, pointA, pointB)
  iIndex <- iBegin
  maxAngle <- Angle(pointA, boundLinePointArray [iBegin], pointB)
  for i in iBegin + 1: boundLinePointArray.size
  angle <- Angle(pointA, boundLinePointArray [i], pointB)
  if angle > maxAngle
    maxAngle <- angle
    iIndex = i
  return iIndex

// input: boundLinePointArray ~ points on the boundary line
//          faultLinePointArray ~ points on the fault line
// output: triangles between boundLinePointArray and faultLinePointArray
Function Reconstruction(boundLinePointArray, faultLinePointArray)
  j <- 0
  for i in 0:FaultLinePointArray.size
    pi <- faultLinePointArray [i]
  pi1 <- faultLinePointArray[i + 1]
  pj <- boundLinePointArray[j]
  if not Intersects(line(pj, pi1), boundLinePointArray)
    k <- FindMaxAngle(boundLinePointArray, j, pi, pi1)
    if k == j
        triArray.add(AddTri(i, i + 1, j))
    else //if k > j
        for m in j:k
            triArray.add(AddTri(i, m, m + 1))
            triArray.add(AddTri(i, i + 1, k))
        LOPswapping(triArray[triArray.size-1], triArray[triArray.size-2])
    j = k
  return triArray
```

Appendix A. Supplementary data

Supplementary data to this article can be found online at https://doi.org/10.1016/j.cageo.2018.12.008.

References

Turk, G., O'Brien, J.F., 2002. Modelling with implicit surfaces that interpolate. ACM Trans. Graph. 21, 855–873. https://doi.org/10.1145/571647.571650.

Bianchi Fasani, G., Bozzano, F., Cardarelli, E., Cercato, M., 2013. Underground cavity investigation within the city of Rome (Italy): a multi-disciplinary approach combining geological and geophysical data. Eng. Geol. 152, 109–121. https://doi.org/10.1016/j.enggeo.2012.10.006.

Bloomenthal, J., 1988. Polygonization of implicit surfaces. Comput. Aided Geomet. Des. 5, 341–355. https://doi.org/10.1016/0167-8396(88)90013-1.
Boisvert, J.B., Deutsch, C.V., 2011. Programs for kriging and sequential Gaussian simulation with locally varying anisotropy using non-Euclidean distances. Comput. Geosci. 37, 495–510. https://doi.org/10.1016/j.cageo.2010.03.021.
Carr, J.C., Beatson, R.K., Cherrie, J.B., 2001. Reconstruction and representation of 3D objects with radial basis functions. In: Proceedings of the 28th Annual Conference on Computer Graphics and Interactive Techniques, pp. 67–76. https://doi.org/10.1145/383259.383266.
Caumon, G., Collon-Drouaillet, P., Le Carlier De Veslud, C., Viseur, S., Sausse, J., 2009. Surface-based 3D modeling of geological structures. Math. Geosci. 41, 927–945. https://doi.org/10.1007/s11004-009-9244-2.
Collon, P., Steckiewicz-Laurent, W., Pellerin, J., Laurent, G., Caumon, G., Reichart, G., Vaute, L., 2015. 3D geomodelling combining implicit surfaces and Voronoi-based remeshing: a case study in the Lorraine Coal Basin (France). Comput. Geosci. 77, 29–43. https://doi.org/10.1016/j.cageo.2015.01.009.
Cowan, E.J., et al., 2003. Practical implicit geological modelling. In: Fifth International Mining Geology Conference. Australian Institute of Mining and Metallurgy Bendigo, Victoria, pp. 89–99.
Cowie, P.A., Shipton, Z.K., 1998. Fault tip displacement gradients and process zone dimensions. J. Struct. Geol. 20 (8), 983–997. https://doi.org/10.1016/S0191-8141(98)00029-7.
de Rienzo, F., Oreste, P., Pelizza, S., 2008. Subsurface geological-geotechnical modelling to sustain underground civil planning. Eng. Geol. 96, 187–204. https://doi.org/10.1016/j.enggeo.2007.11.002.
Fasshauer, Gregory, E., 2007. Meshfree Approximation Methods with Matlab:(With CD-ROM), vol. 6 World Scientific Publishing Co Inc.
Franke, R., 1982. Scattered data interpolation: tests of some methods. Math. Comput. 38, 181. https://doi.org/10.1090/S0025-5718-1982-0637296-4. 181.
Guo, J., Wu, L., Zhou, W., Jiang, J., Li, C., 2016. Towards automatic and topologically consistent 3D regional geological modeling from boundaries and attitudes. ISPRS Int. J. Geo-Inf. 5, 17. https://doi.org/10.3390/ijgi5020017.
Hassen, I., Gibson, H., Hamzaoui-azaza, F., Negro, F., Rachid, K., 2016. 3D geological modeling of the Kasserine Aquifer System , Central Tunisia : new insights into aquifer-geometry and interconnections for a better assessment of groundwater resources. J. Hydrol. 539, 223–236. https://doi.org/10.1016/j.jhydrol.2016.05.034.
Hillier, M.J., Schetselaar, E.M., de Kemp, E.A., Perron, G., 2014. Three-dimensional modelling of geological surfaces using generalized interpolation with radial basis functions. Math. Geosci. 46, 931–953. https://doi.org/10.1007/s11004-014-9540-3.
Hsieh, Cheng-Tiao, 2012. An efficient development of 3D surface registration by Point Cloud Library (PCL). In: Intelligent Signal Processing and Communications Systems (ISPACS), 2012 International Symposium on. IEEE, https://doi.org/10.1109/ISPACS.2012.6473587.
Kaufmann, O., Martin, T., 2009. Reprint of “3D geological modelling from boreholes, cross-sections and geological maps, application over former natural gas storages in coal mines”. Comput. Geosci. 35, 70–82. https://doi.org/10.1016/S0098-3004(08)00227-6.
Knight, R.H., Lane, R.G., Ross, H.J., Abraham, a P.G., Cowan, J., 2007. Implicit ore delineation. Proc. Explor. 07 fifth decenn. Int. Conf. Miner. Explor. 1165–1169.
Lawson, C.L., 1977. Software for c 1, surface interpolation. Math. Software 161–194. https://doi.org/10.1016/B978-0-12-587260-7.50011-X.
Li, X., Li, P., Zhu, H., 2013. Coal seam surface modeling and updating with multi-source data integration using Bayesian Geostatistics. Eng. Geol. 164, 208–221. https://doi.org/10.1016/j.enggeo.2013.07.009.
Lindsay, M.D., Aillères, L., Jessell, M.W., de Kemp, E.A., Betts, P.G., 2012. Locating and quantifying geological uncertainty in three-dimensional models: analysis of the Gippsland Basin, southeastern Australia. Tectonophysics 546–547, 10–27. https://doi.org/10.1016/j.tecto.2012.04.007.
Martin, R., Boisvert, J.B., 2017. Iterative refinement of implicit boundary models for improved geological feature reproduction. Comput. Geosci. 109, 1–15. https://doi.org/10.1016/j.cageo.2017.07.003.
Möller, Tomas, Trumbore, Ben, 2005. Fast, minimum storage ray-triangle intersection. ACM SIGGRAPH 2, 7. https://doi.org/10.1080/10867651.1997.10487468. ACM.
Narayan, K.S., Sha, J., Singh, A., Abbeel, P., 2015. Range sensor and silhouette fusion for high-quality 3D Scanning. Proc. - IEEE Int. Conf. Robot. Autom. 3617–3624. https://doi.org/10.1109/ICRA.2015.7139701. 2015–June.
Ohtake, Y., Belyaev, A., Seidel, H.P., 2003. A multiscale approach to 3D scattered data interpolation with compactly supported basis functions. Shape Model. Int. 153–161. https://doi.org/10.1109/SMI.2003.1199611.
Rusu, R.B., Cousins, S., 2011. 3D is here: point cloud library (PCL). Proc. - IEEE Int. Conf. Robot. Autom. https://doi.org/10.1109/ICRA.2011.5980567.
Tsai, V.D., 1993. Delaunay triangulations in tin creation: an overview and a linear-time algorithm. Int. J. Geogr. Inf. Syst. 7 (6), 501–524. https://doi.org/10.1080/02693799308901979.
Vollgger, S.A., Cruden, A.R., Ailleres, L., Cowan, E.J., 2015. Regional dome evolution and its control on ore-grade distribution: insights from 3D implicit modelling of the Navachab gold deposit, Namibia. Ore Geol. Rev. 69, 268–284. https://doi.org/10.1016/j.oregeorev.2015.02.020.
Wendland, H., 1995. Piecewise polynomial, positive definite and compactly supported radial functions of minimal degree. Adv. Comput. Math. 4, 389–396. https://doi.org/10.1007/BF02123482.
Wilde, Brandon J., Deutsch, Clayton V., 2012. Kriging and simulation in presence of stationary domains: developments in boundary modeling. In: Geostatistics Oslo 2012. Springer Netherlands, pp. 289–300.
Zhu, L.F., Li, M.J., Li, C.L., Shang, J.G., Chen, G.L., Zhang, B., Wang, X.F., 2013. Coupled modeling between geological structure fields and property parameter fields in 3D engineering geological space. Eng. Geol. 167, 105–116. https://doi.org/10.1016/j.enggeo.2013.10.016.